

Multimaterial Photodetecting Fibers: a Geometric and Structural Study**

By Fabien Sorin, Ayman F. Abouraddy, Nick Orf, Ofer Shapira, Jeff Viens, Jeremy Arnold, John D. Joannopoulos, and Yoel Fink*

The recent development of codrawn metal-insulator-semiconductor photodetecting fiber devices with mesoscopic-scale cross-sectional features has heralded a novel path to optical radiation detection.^[1–8] For the first time, optical detection function may be delivered at length scales and in a mechanically flexible form hitherto associated with optical fibers. At the heart of the fabrication process is the simultaneous reduction of the cross-section and extension of the axial dimensions of a macroscopic preform. Thermal drawing results in extended length scales of functional fiber while maintaining the material composition and transverse geometry throughout. Although beneficial for many applications,^[1,2,5,6] the extended length scales of fiber-devices tend to degrade their performance by raising the noise floor. Our study aims to minimize the noise per unit length by identifying optimal fiber structures and geometries. A comparative study of the responsivity, noise and sensitivity^[9,10] of photodetecting fibers as a function of structural and geometric scaling parameters is performed. A novel thin-film photodetecting fiber device architecture is introduced. Precise control over the submicron scale dimensions affords more than an order of magnitude increase in the fiber-device sensitivity. Potential applications of fiber devices include remote sensing, functional fabrics, and large-area, two-dimensional (2D) and three-dimensional (3D) arrays (or “fiber webs”) capable of optical imaging.^[1,5,6]

The basic structures and scaling parameters of the fibers discussed in this paper are illustrated in Figure 1. The mesoscopic-scale fiber devices are produced from a macroscopic-scale preform, having the desired device structure albeit at macroscopic dimensions, by a thermal drawing technique ((a1), see Experimental). This process enables the incorporation of materials with widely disparate electrical and optical properties into hundreds of meters of fiber (a2).^[1,2] Two basic fiber-device structures are considered here and are contrasted in Figure 1b and c. The first structure^[1,2] consists of a solid amorphous semiconducting core contacted with four metallic conduits (tin) and a protective polymer cladding, poly(ether sulfone) (PES) that encapsulates the device while simultaneously imparting mechanical strength and flexibility to the fiber. Figure 1b shows a schematic drawing (b1), a scanning electron microscope (SEM) micrograph (b2) of the cross section, and a longitudinal section of this fiber device. The drawing process maintains the ratio of the solid-core diameter d , the scaling parameter we investigate, to the fiber outer diameter. The second fiber device is similar to the above described device except that the photoconducting element is a thin film (of the same material used in the solid-core fiber) supported by an inner polymer tube. Figure 1c shows a schematic drawing (c1), an SEM image (c2) of the cross section, and a longitudinal section of this fiber device. This new structure allows for two independent scaling parameters to be varied: the diameter of the thin film d (corresponding to the diameter of the above described solid-core device) and the film thickness t . We show that this additional degree of freedom enables the design of photodetecting fibers with enhanced sensitivities. The amorphous semiconductor used in this paper is a chalcogenide glass having the formula $\text{As}_{40}\text{Se}_{54}\text{Te}_6$,^[11] although the composition can be changed to optimize the performance according to the application at hand and the scaling trends reported here are essentially *independent* of the semiconductor used.

In our investigation of the scaling effects on fiber device performance, we are interested in four quantities: the dark current, the noise current, the photocurrent, and the device sensitivity. The dark current I_{dark} is defined as the *average* current in the fiber when no photons are incident on it. We define the noise current i_N as the *standard deviation* of the current fluctuations around I_{dark} . The photocurrent I_{ph} is the *average* current under some predefined illumination condition. Finally, the sensitivity s is defined as the photogenerated current divided by the noise current, $s = \frac{I_{\text{ph}} - I_{\text{dark}}}{i_N}$.

[*] Prof. Y. Fink, F. Sorin, N. Orf, J. Viens
Department of Materials Science and Engineering
Massachusetts Institute of Technology
Cambridge MA 02139 (USA)
E-mail: yoel@mit.edu

Prof. Y. Fink, Dr. A. F. Abouraddy, F. Sorin, O. Shapira, J. Arnold,
Prof. J. D. Joannopoulos
Research Laboratory of Electronics, Massachusetts Institute of
Technology
Cambridge, MA 02139 (USA)

O. Shapira, J. Arnold
Department of Electrical Engineering and Computer Science
Massachusetts Institute of Technology
Cambridge MA 02139 (USA)

Prof. Y. Fink, Prof. J. D. Joannopoulos
Institute for Soldier Nanotechnologies MIT,
Cambridge, MA 02139 (USA)

[**] The authors thank Drursen Saygin-Hinczewski, Mehmet Bayindir, Gilles Benoit, Ismaila Dabo and Zachary Ruff for their help at different stages of the project. This work was supported by US Army ISN, ONR, AFRL, NSF, US DOE and DARPA. This work was also supported in part by the MRSEC Program of the National Science Foundation. We also thank the RLE and CMSE for their support.

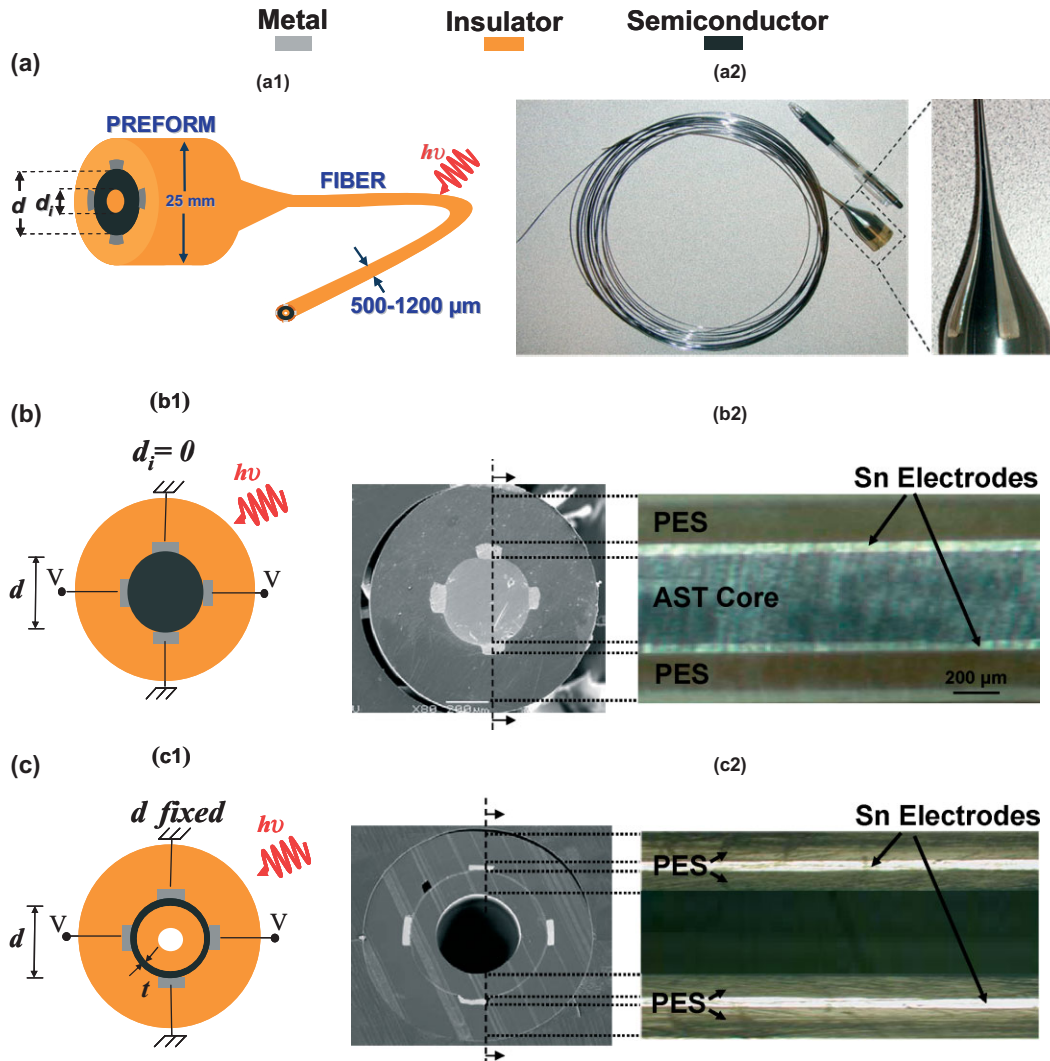


Figure 1. Geometry and structure of mesoscopic photodetecting fiber devices. a) A macroscopic preform is drawn down to a mesoscopic fiber (a1). Meters-long fiber devices (a2) are produced from the preform (the neckdown region of the preform is shown in the inset). b) (b1) Schematic cross-section of a solid-core fiber device showing the electrical connections to an external circuit and the relevant device parameters. (b2) Scanning electron microscope images of cross section and image of a longitudinal section of the fiber device. c) (c1) Schematic cross-section of a thin-film fiber device showing the electrical connections to an external circuit and the relevant device parameters. (c2) Scanning electron microscope images of cross section and image of a longitudinal section of the thin-film fiber device (the thin film is not visible in the longitudinal section).

We start our investigation by considering the effect of fiber length L on the abovementioned parameters for the case of solid-core fibers. Measurements reveal that I_{dark} increases linearly with L as expected (Fig. 2a). A simple analytical model that considers only the dark-current fluctuations due to Johnson and generation-recombination noise^[9,10] (neglecting the effect of $1/f$ noise at low frequencies) and adapted to our particular geometry indicates that the amplitude of i_N is proportional to $\sqrt{I_{\text{dark}}}/d$, and thus $i_N \propto \sqrt{L}$ (Fig. 2b). An analysis of noise in amorphous semiconductors^[12] also leads to a same dependence of noise on L and d when adapted to our geometry. On the other hand, $I_{\text{ph}} - I_{\text{dark}}$ is independent of L (if the fiber is longer than the illumination spot), and consequently $s \propto 1/\sqrt{L}$, i.e., the sensitivity drops as the fiber length increases.

We now turn to the dependence of the solid-core fiber device performance on the core diameter d . We find that I_{dark} , counter-intuitively, is independent of core diameter (Fig. 2c). This result may be elucidated by considering the following symmetry argument. While the electric-field distribution $\vec{E}^d(r, \theta)$ for diameter d becomes $\vec{E}^D(r, \theta) = \frac{d}{D} \vec{E}^d(R, \theta)$ when the diameter is D , this scaling is balanced by a scaling of the integration area. A reduction in diameter then yields an increase of electric field but also decreases the integration path of the current density in the radial direction by the same factor, resulting in I_{dark} being independent of d .

While I_{dark} results from contributions from the full volume of the photoconducting core, the volume that contributes to $I_{\text{ph}} - I_{\text{dark}}$ upon external illumination is limited to a shell having a thickness equal to several penetration depths of the inci-

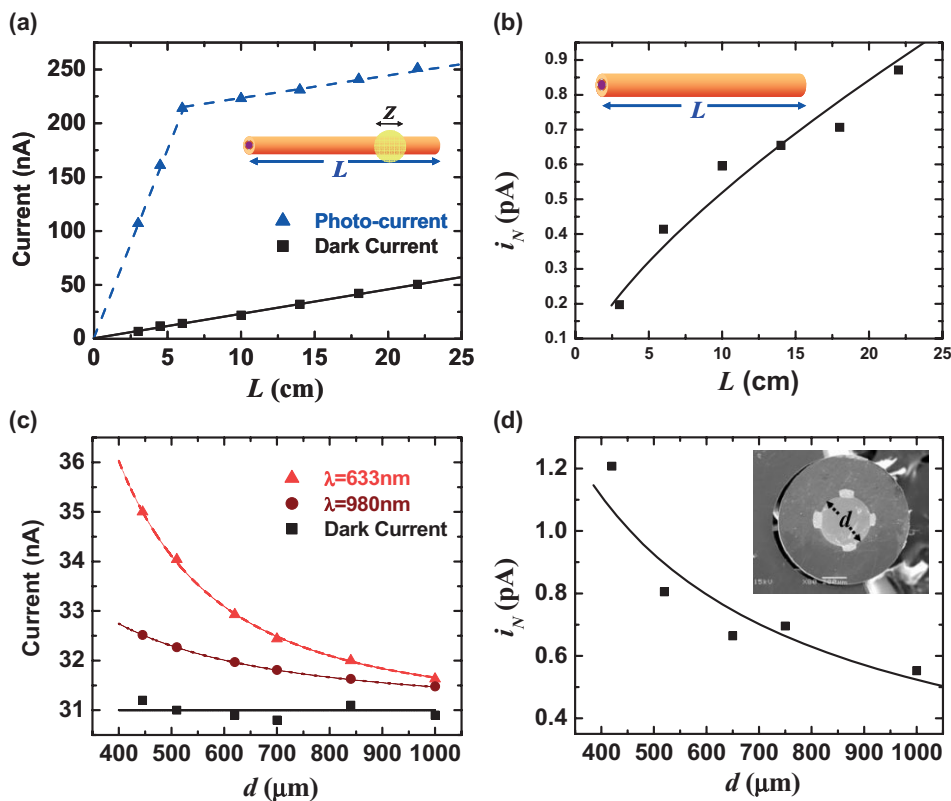


Figure 2. Theory prediction (solid lines) and experimental results (dots) of the scaling trends of solid-core fiber devices. a) Dependence of the dark current and photocurrent (white light illumination over a spot of diameter z) on the fiber length L . b) Dependence of noise current on fiber length L . c) Dependence of dark current and photocurrent (at two wavelengths) on the diameter of the fiber core d . d) Dependence of noise current on d .

dent wavelength, which is typically much smaller than the core sizes of the fabricated devices. In this case $I_{\text{ph}} - I_{\text{dark}}$ is dependent on the fiber diameter, and one may show analytically that it is in fact *inversely proportional* to d^2 for fixed number of incident photons of a given wavelength. This scaling argument was verified quantitatively using the phenomenological approach described in Ref.^[13] taking into account the particular geometry and structure of the fiber device. Using a finite element modeling method (with FEMLAB[®]) to calculate the distribution of the electric field in our structure and assuming boundary conditions where no charges are generated at the interfaces between the polymer and the glass, we find that the dependence of $I_{\text{ph}} - I_{\text{dark}}$ on d confirms the behavior described above.

The result was verified experimentally by measuring I_{ph} for fibers having different d ranging from 440 to 1000 μm under fixed illumination conditions. The spectral dependence of I_{ph} was investigated at two wavelengths, $\lambda = 633$ nm (He-Ne laser) and $\lambda = 980$ nm (laser diode). The penetration depths δ used for the simulations, obtained from measuring the imaginary part of the glass refractive index, are $\delta(\lambda = 633 \text{ nm}) = 100$ nm and $\delta(\lambda = 980 \text{ nm}) = 425$ μm . Figure 2c demonstrates that the results of our model agree well with the experimental data. Finally, in Figure 2d we plot i_N as a function of d , showing the

expected inverse proportionality. Thus while smaller diameters afford a larger I_{ph} ($I_{\text{ph}} - I_{\text{dark}} \propto 1/d^2$) they also result in a larger i_N ($i_N \propto 1/d$); nevertheless, the sensitivity increases for smaller fiber diameters $s \propto 1/d$. The background noise resulting from the extended length of a photodetecting fiber device is hence compensated by a reduction of its cross-sectional dimensions. An intriguing observation can already be made based on this result. Indeed, attaining smaller diameters lowers the cost and weight of fiber unit length from the same preform while increasing the fiber mechanical flexibility, thus allowing the fiber to be woven into a fabric. Our study shows that, counter intuitively, thinner fibers are *also more sensitive*, which adds to our motivation for producing fibers with even smaller diameters.

We now turn to an alternative strategy: replacing the solid core with a thin-film photoconducting structure (Fig. 1c). A striking advantage of the new thin-film structure compared to its solid-core counterpart is the significant reduction of I_{dark} and hence device noise per unit length, as exemplified in Figure 3a, where i_N of the solid-core and thin-film fibers (both having the same diameter d) are plotted as a function of L . The drop in I_{dark} for a thin-film structure results from removal of most of the bulk of the glass contributing to I_{dark} in the solid-core case. On the other hand, $I_{\text{ph}} - I_{\text{dark}}$ remains the *same* in

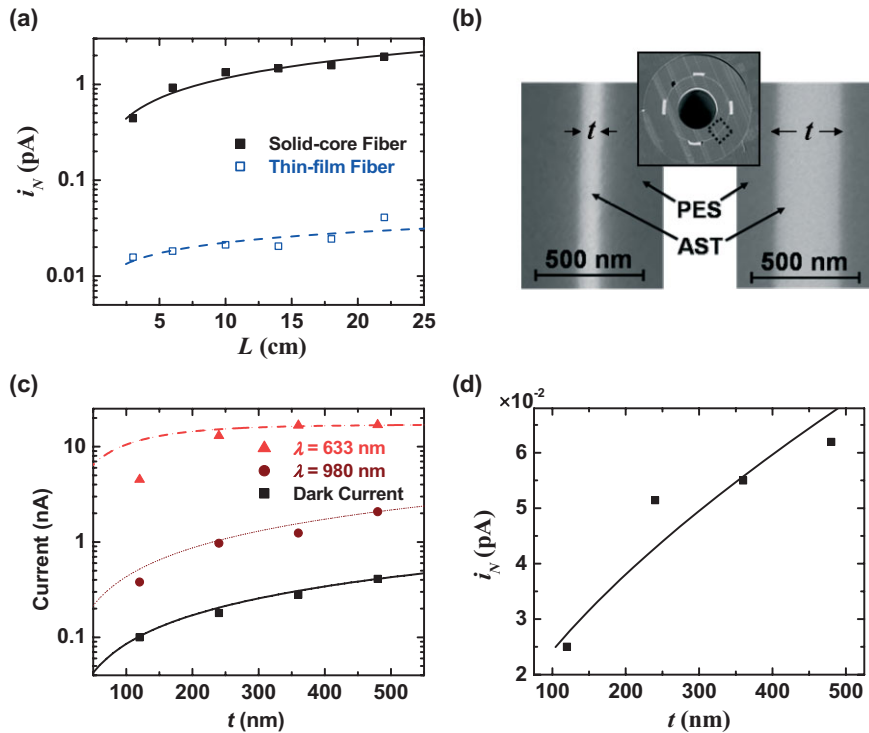


Figure 3. Theory prediction (solid lines) and experimental results (dots) of the scaling trends of thin-film fiber devices. a) Comparison of the dependence of the noise current of solid-core and thin-film fiber devices having the same diameter. b) SEM images of the thin-film devices having thicknesses of 120 and 360 nm showing. c) Dependence of the dark current and photocurrent (at two wavelengths) on thin-film thickness t . d) Dependence of the noise current on t .

both structures if the film thickness exceeds a few penetration depths at the illumination wavelength. For the thin-film structure, I_{ph} is given by a simple formula:

$$I_{ph} - I_{dark} \propto T \cdot E \cdot (1 - e^{-t/\delta}) \quad (1)$$

where T represents the fraction of externally incident photons that reach the thin film, t the film thickness, δ the penetration depth, and E the electric field intensity. The third term in Equation 1 is proportional to the fraction of photons reaching the thin film that generate photocharges in it. We have assumed a uniform field throughout the thin film, an approximation we have found valid over the range of considered thicknesses using our computational model.

In order to study the effect of the film thickness on the performance of this new structure, we fabricated 4 preforms having identical dimensions and structures while only varying the thickness of the incorporated thin film. The preforms were drawn down by the same reduction factor resulting in final film thicknesses of 120, 240, 360, and 480 nm. On Figure 3b we show SEM images of thin-film devices with $t = 120$ nm and $t = 360$ nm. These micrographs demonstrate the precise control over the thickness of sub-micrometer-thick photodetecting films spanning the entire fiber length (hundreds of meters). We find that the dependence of $I_{ph} - I_{dark}$ on t (Fig. 3c) follows closely the expected form given $1 - e^{-t/\delta}$ in Equation 1.

A notable exception is I_{ph} for the thinnest film (120 nm) at the shorter wavelength. We believe that this loss of responsivity (i.e., photocurrent per incident power) is due to surface roughness which is more pronounced as the feature sizes are reduced and the film thickness becomes comparable to the penetration depth. Surface roughness reduces the photocurrent since most of the free carriers in this case have lower drift mobility. This is corroborated by the observation that the responsivity of thin-film devices is smaller (by a factor of 2 to 3) than solid-core structures of similar glass composition. In addition to surface roughness we believe that the thin-film composition is more inhomogeneous than the bulk glass due to dissociation during evaporation and rapid cooling under vacuum.^[14,15] This leads to an increase in disorder and of the density of localized states in the band tail reducing further the free-carrier average drift mobility.^[16,17]

From Figure 3 we see that increasing the film thickness increases $I_{ph} - I_{dark} \propto 1 - e^{-t/\delta}$ and $i_N \propto \sqrt{i}$. It is then possible to engineer the material (δ) and the film thickness t to maximize the sensitivity $s \propto (1 - e^{-t/\delta})/\sqrt{i}$ of the device at a given wavelength. For an illumination at 674 nm, corresponding to $\delta(\lambda = 674 \text{ nm}) = 150$ nm, this function is maximal for a film thickness of 240 nm. This extra independent degree of freedom in the fiber structural design is of significant advantage for applications where one is constrained on the fiber external dimensions (d and L).

Figure 4, where the spectral dependence of the sensitivity for solid-core and thin-film fiber devices are contrasted, summarizes many features discussed in this paper. In the solid-core case, s is relatively constant over a very wide spectral range (and hence penetration depths) with two notable exceptions. At small penetration depth (short wavelength), light is absorbed close to the surface of the core where the electric field is maximal, leading to an increase in I_{ph} and hence s . A drop in s occurs at very large penetration depth (long wavelength) when δ becomes comparable to the diameter d . In the thin-film case, a drop in s occurs when the thickness t becomes comparable to δ since a large fraction of incident photons go unabsorbed. Nevertheless, thin-film fibers have a sensitivity of more than an order of magnitude better than solid-core fibers at shorter penetration depths. The judicious choice of materials, structure and dimensions can hence lead to significant improvement in device performance for a given application.

To give an idea of the performance of such fiber devices, the Noise Equivalent Power (NEP) which is the illuminating

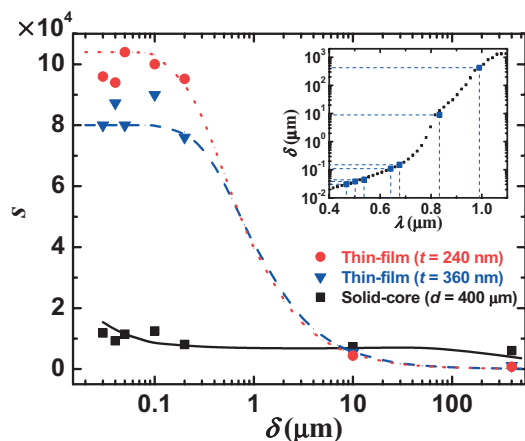


Figure 4. Comparison of the sensitivity s for solid-core and thin-film fiber devices as a function of penetration depth of the incident radiation, or equivalently the radiation wavelength (the inset shows the dependence of the penetration depth on wavelength for the amorphous semiconductor glass used in this paper).

power for which the sensitivity is equal to one,^[9,10] was measured to be of approximately $25 \text{ nW cm}^{-1/2}$ for a fiber with film thickness of 240 nm illuminated at 674 nm, more than an order of magnitude lower than for its solid-core-fiber counterpart. Note also that other structural modifications such as the addition of electrodes, the reduction of their spacing, the addition of anti-reflective coatings, packaging of multiple photodetecting elements into a single fiber, post-drawing crystallization of the amorphous semiconductor, and also the use of higher voltage bias can significantly improve the device performance. Nevertheless, the scaling effects are independent of both the glass used and the type of improvements listed above which make the conclusions drawn in this study general and robust.

The improvement in performance of the new photodetecting thin-film structure allows us to extend the range of fiber-based-device applications. The large-area fiber-webs constructed of solid-core fibers used as large interacting screens or in lensless imaging systems are intriguing applications of photodetecting fiber-devices.^[1,2,5,6] The low sensitivity of these fibers necessitated the use of high incident optical power, 1.5 W in the case of the lensless imaging system to reconstruct an image from an illuminated object.^[5,6] A grid with the same size constructed of higher sensitivity thin-film fibers could perform the same task with incident power lower than 100 mW, which can be provided by a simple laser diode. Moreover, these large interactive screens, or even functional fabrics, could respond to even weaker light sources such as laser pointers which make them useful for real-world applications. Our study also has striking implications with respect to the increase of fiber-web size possible using thin-film devices while maintaining the same sensitivity performance of previously published arrays. Since the sensitivity is inversely proportional to \sqrt{L} , a 100 m long thin-film fiber can detect a light beam with the same sensitivity as a 1 m long solid-core fiber

if a modest 10 times improvement in sensitivity is achieved. This means that if we could cover a 1 m^2 photodetecting area with a required level of sensitivity with our previously reported solid-core fiber grid, we can now build a thin-film-fiber grid of $10\,000 \text{ m}^2$ of photodetecting area while maintaining the same sensitivity.

Another significant aspect of thin-film structures is that they are amenable to dense integration of further optoelectronic devices in the same fiber. While passive structures (such as external Bragg mirrors^[1]) may be incorporated in solid-core fibers, the addition of other photodetecting devices in the same fiber cannot be achieved in a straightforward fashion. The novel fiber device structure described in this paper paths the way to integrating multiple devices in a single multifunctional fiber.

In summary we studied the relation between the geometry and sensitivity of cylindrical fiber photodetectors. Scaling laws for these structures were derived and geometric approaches to increased sensitivity were introduced. Specifically it was shown that decreasing the fiber photodetector diameter results in a linear increase in sensitivity. A new thin film fiber photodetector was designed and fabricated and measured to exhibit lower noise level (~ 1 order of magnitude) than its solid core predecessor. These photodetecting fibers are expected to enable large area optical detection for a variety of applications.

Experimental

Glass Synthesis and Thin-Film Processing (Fig. 5A1): The chalcogenide glass ($\text{As}_{40}\text{Se}_{54}\text{Te}_6$) rods, 10 mm in diameter and 15 cm long, were prepared from high-purity As, Se, and Te elements (Alfa Aesar) using conventional sealed-ampoule melt-quenching techniques [18]. The materials were weighed and placed into a quartz tube under a dry nitrogen atmosphere. The elements were heated at 250°C under vacuum for 2 h to remove water and surface oxides. The ampoule was formed by sealing the tube under vacuum ($\sim 10^{-5}$ Torr). It was then heated to 750°C at a rate of 2°C min^{-1} in a rocking furnace for 18 h, while being held vertically, and then rocked for 6 h to increase mixing and homogenization. The glass liquid was cooled to 600°C and then quenched in cold water. Subsequently, it was annealed for 30 min near the glass-transition temperature before gradually cooling to room temperature. The thin films were obtained by thermal evaporation of glass chunks onto a $50 \mu\text{m}$ thick PES sheet under high vacuum ($\sim 10^{-6}$ Torr).

Preform Preparation and Fiber Drawing (see Fig. 5A and B): A macroscopic cylindrical preform, 25 mm in diameter and 20 cm long, was consolidated for 60 min at 260°C under vacuum (10^{-3} Torr) in a three-zone horizontal tube furnace while rotating the preform around its axis. Subsequently, the preform was drawn into 10 s of meters of fiber in a three-zone vertical tube furnace with the top-zone temperature at 190°C , the middle-zone temperature at 295°C and the lower zone at 150°C .

Glass Optical Properties and Electrical Measurements: The real n and imaginary k parts of the refractive index for the glass were measured using a broadband spectroscopic ellipsometer (Sopra GES-5), from which the penetration depth was extracted using the formula $\delta = \lambda/4\pi k$. Samples were prepared by thermal evaporation on silica substrates, followed by annealing for an hour at 180°C . Electrical contacts for the fibers were made by locally removing the polymer cladding at one end of the fiber and soldering a wire to the exposed tin electrodes, allowing for the fiber to be connected to external electron-

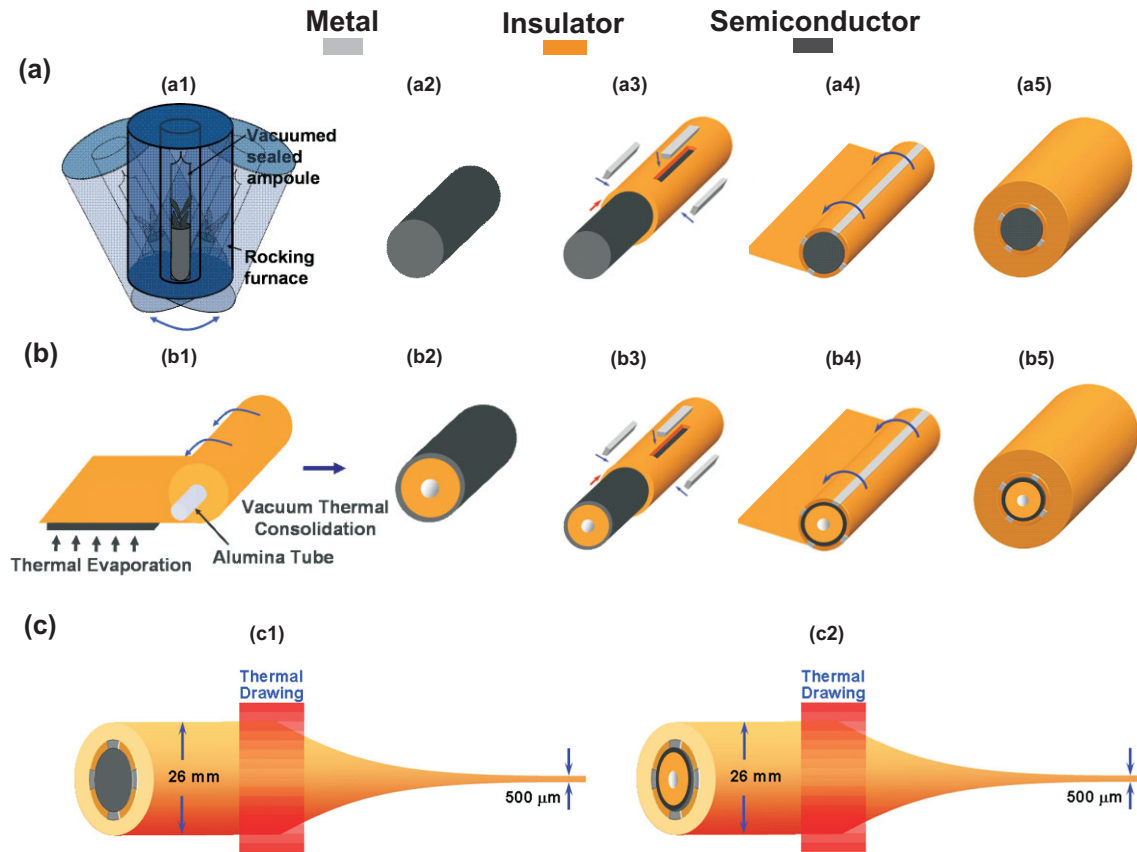


Figure 5. Fabrication steps for producing solid-core and thin-film fiber devices from a macroscopic preform. a) Producing a solid-core fiber device. A chalcogenide rod (a2) is slid into a polymer tube where rectangular spaces have been cut to place the Sn electrodes (a3). The structure is then encapsulated in a polymer cladding (a4) and consolidated to obtain a macroscopic preform (a5) (see text). b) Producing a thin-film fiber device. Chalcogenide glass is thermally evaporated on a polymer sheet (b1) that is rolled and consolidated to obtain a polymer tube with an outer layer of controlled thickness of glass (b2). The structure is then encapsulated in a polymer cladding (b4) and consolidated to obtain a macroscopic preform (b5) (see text). c) Thermal drawing of macroscopic preforms yields the mesoscopic solid-core and thin-film fiber devices (see text).

ic circuitry. 50 V dc was applied to the fibers for all electronic measurements. The dark current I_{dark} and photocurrent I_{ph} were measured with a pico-ameter (Keithley 6487). The noise current i_N was measured by carefully shielding the fibers from the environment, recording the current over an extended period of time (typically 10 min.), and statistical analysis of the amplitude of the fluctuations.

Received: January 21, 2007

Revised: May 22, 2007

[1] M. Bayindir, F. Sorin, A. F. Abouraddy, J. Viens, S. D. Hart, J. D. Joannopoulos, Y. Fink, *Nature* **2004**, *431*, 826.
 [2] M. Bayindir, A. F. Abouraddy, F. Sorin, J. D. Joannopoulos, Y. Fink, *Opt. Photon. News* **2004**, *15*, 24.
 [3] M. Bayindir, O. Shapira, D. Saygin-Hinczewski, J. Viens, A. F. Abouraddy, J. D. Joannopoulos, Y. Fink, *Nat. Mater.* **2005**, *4*, 820.
 [4] M. Bayindir, A. F. Abouraddy, J. Arnold, J. D. Joannopoulos, Y. Fink, *Adv. Mater.* **2006**, *18*, 845.
 [5] A. F. Abouraddy, O. Shapira, M. Bayindir, J. Arnold, F. Sorin, D. Saygin-Hinczewski, J. D. Joannopoulos, Y. Fink, *Nat. Mater.* **2006**, *5*, 532.
 [6] A. F. Abouraddy, O. Shapira, M. Bayindir, J. Arnold, J. D. Joannopoulos, Y. Fink, *Opt. Photon. News* **2006**, *17*, 21.

[7] Bayindir, A. F. Abouraddy, O. Shapira, J. Viens, D. Saygin-Hinczewski, F. Sorin, J. Arnold, J. D. Joannopoulos, Y. Fink, *IEEE J. Sel. Top. Quantum Electron.* **2006**, *12*(6), 1202.
 [8] A. F. Abouraddy, M. Bayindir, G. Benoit, S. D. Hart, K. Kuriki, N. Orf, O. Shapira, F. Sorin, B. Temelkuran, Y. Fink, *Nat. Mater.* **2007**, *6*, 336.
 [9] E. Rosencher, B. Vinter, *Optoelectronics*, Cambridge University Press, New York **2002**.
 [10] R. H. Kingston, *Detection of Optical and Infrared Radiation*, Springer, Berlin, New York **1978**.
 [11] Z. U. Borisova, *Glassy Semiconductors*, Plenum, New York **1981**.
 [12] S. Reynolds, C. Maine, M. J. Rose, *J. Non-Cryst. Solids* **1998**, *227–230*, 233.
 [13] D. Ritter, E. Zeldov, K. Weiser, *Phys. Rev. B* **1988**, *38*(12), 8296.
 [14] A. Schulte, C. Rivero, K. Richardson, K. Turcotte, V. Hamel, A. Vileneuve, T. Galsitan, R. Vallee, *Opt. Commun.* **2001**, *198*, 125.
 [15] R. Ston, M. Vlcek, H. Jain, *J. Non-Cryst. Solids* **2003**, *326–327*, 220.
 [16] N. F. Mott, E. A. Davis, *Electronic Processes in Non-Crystalline Materials, Conduction in Non-crystalline Materials*, Oxford University Press, New York **1979**.
 [17] J. M. Marshall, *Rep. Prog. Phys.* **1983**, *46*, 1235.
 [18] V. K. Tikhomirov, D. Furniss, A. B. Seddon, J. A. Savage, P. D. Mason, D. A. Orchard, K. L. Lewis, *Infrared Phys. Technol.* **2004**, *45*, 115.